PNAS RESEARCH ARTICLE | BIOPHYSICS AND COMPUTATIONAL BIOLOGY

Three-dimensional architecture of ESCRT-III flat spirals on the membrane

Mingdong Liu[a,b,c,d], Yunhui Liu[c], Tiefeng Song[e,f], Liuyan Yang[g], Lei Qi[b,h], Yu-Zhong Zhang[g], Yong Wang[e,f], and Qing-Tao Shen[a,b,c,d,1]

Edited by Robert Stroud, University of California, San Francisco, CA; received November 1, 2023; accepted April 1, 2024

The endosomal sorting complexes required for transport (ESCRTs) are responsible for membrane remodeling in many cellular processes, such as multivesicular body biogenesis, viral budding, and cytokinetic abscission. ESCRT-III, the most abundant ESCRT subunit, assembles into flat spirals as the primed state, essential to initiate membrane invagination. However, the three-dimensional architecture of ESCRT-III flat spirals remained vague for decades due to highly curved filaments with a small diameter and a single preferred orientation on the membrane. Here, we unveiled that yeast Snf7, a component of ESCRT-III, forms flat spirals on the lipid monolayers using cryogenic electron microscopy. We developed a geometry-constrained Euler angle–assigned reconstruction strategy and obtained moderate-resolution structures of Snf7 flat spirals with varying curvatures. Our analyses showed that Snf7 subunits recline on the membrane with N-terminal motifs α0 as anchors, adopt an open state with fused α2/3 helices, and bend α2/3 gradually from the outer to inner parts of flat spirals. In all, we provide the orientation and conformations of ESCRT-III flat spirals on the membrane and unveil the underlying assembly mechanism, which will serve as the initial step in understanding how ESCRTs drive membrane abscission.

ESCRTs | flat spirals | cryo-EM | Euler angles | geometric constraints

Significance

The endosomal sorting complexes required for transport (ESCRTs) play a vital role in many cellular processes by helping to reshape membranes, and dysfunction of ESCRTs is associated with many human diseases, such as cancer and neurodegenerative diseases. ESCRT-III, the most abundant ESCRT subunit, assembles into flat spirals as the primed state to initiate membrane invagination. However, the three-dimensional architecture of ESCRT-III flat spirals remained vague for decades due to structural heterogeneity and preferred orientation. In this work, we developed a geometry-constrained Euler angle–assigned reconstruction strategy and demonstrated the orientation and conformations of ESCRT-III flat spirals on the membrane. Our results unveil the assembly mechanism of ESCRT-III flat spirals on the membrane, which helps understand how ESCRT-III drives membrane abscission.

The endosomal sorting complex required for transport (ESCRT) is a conserved molecular machinery among the Archaea, Bacteria, and Eukaryota (1–6). ESCRTs were first identified as the sole machinery involved in membrane budding away from the cytosol (negative curvature) (*SI Appendix*, Fig. S1*A*) and get involved in many classical cellular processes, ranging from multivesicular body (MVB) biogenesis (7, 8), autophagy (9, 10), cytokinetic abscission (11, 12), neuron pruning (13, 14), and viral budding (15, 16). Recently, a subset of ESCRTs, such as CHMP1B-IST1, were seen to form a double-layer helix and coat the outer surface of membrane tubes, leading to membrane budding toward the cytosol (positive curvature) (*SI Appendix*, Fig. S1*B*) (17). New functions of ESCRTs are emerging quickly, including tubular endosomal traffic from the endoplasmic reticulum (ER) to lysosomes (18) and lipid droplets to peroxisomes (19) and the release of newly formed peroxisomes from the ER (20). Dysfunction of ESCRTs is associated with many human diseases, such as cancer and neurodegenerative diseases (21, 22).

To fulfill these diverse activities, the ESCRT machinery comprises ALIX, ESCRT-I, ESCRT-II, ESCRT-III, and VPS4 subcomplexes (23). ALIX and ESCRT-I/ESCRT-II proteins are early-acting ESCRT factors that recognize ubiquitinated cargoes and further nucleate ESCRT-III proteins (24–31). As the most abundant subunits, ESCRT-III proteins polymerize to catalyze the membrane abscission. The AAA-ATPase Vps4 is finally recruited to ESCRT-III enriched sites, consuming ATP to disassemble ESCRT-III filaments for recycling (32–34).

In yeast, ESCRT-III comprises four core subunits (Vps20, Snf7, Vps24, and Vps2) and three accessory components (Did2, Vps60, and Ist1) (*SI Appendix*, Figs. S1 *C, D* and S2) (35, 36). All these ESCRT-III proteins share similar secondary structures containing four α-helices (α1–α4) on their N terminus, with α1 and α2 forming a hairpin (37, 38). Purified ESCRT-III subunits are usually monomeric and stay in a closed autoinhibited conformation with its α5 on the C-terminal packing against the tip of the α1–α2 hairpin (39–41). Upon activation via membranes or upstream activators, or artificially through truncation of their C-terminal elements, most ESCRT-III proteins adopt an open conformation with α2 and α3 fusing into a long α2/3 helix (*SI Appendix*, Fig. S2) (42, 43) and further polymerize into either flat spirals, conical spirals, or helical tubes (17, 34, 44–49). The sequential polymerization of ESCRT-III subunits from Snf7 to Vps24, Vps2, Did2, and finally Ist1, driven by Vps4, triggers structural transitions of ESCRT-III polymers and induces membrane deformation and fission, which reaches a dome model to describe the tandem abscission process (50, 51).

The dome model postulates that ESCRT-III proteins assemble in a hemispherical dome shape from flat spirals at the neck location (52). This dome guides the closure of the neck by promoting membrane-protein adhesion after the formation of helical

Author contributions: Q.-T.S. designed research; M.L. and Q.-T.S. performed research; M.L., Y.L., and Q.-T.S. analyzed data; Y.L., T.S., L.Y., L.Q., Y.-Z.Z., and Y.W. contributed new reagents/analytic tools; and Q.-T.S. wrote the paper.

The authors declare no competing interest.

This article is a PNAS Direct Submission.

[1]To whom correspondence may be addressed. Email: shenqt@sustech.edu.cn.

This article contains supporting information online at https://www.pnas.org/lookup/suppl/doi:10.1073/pnas.2319115121/-/DCSupplemental.

Published May 6, 2024.

tubes. In the late stage of ESCRT-mediated membrane abscission, human Vps2-Vps24 heterodimers assemble into the helical tube, coated with a membrane, and position their short N-terminal motifs α0 for membrane interaction (34, 53, 54). Distinct from Vps2-Vps24, CHMP1B forms the inner layer of the CHMP1B-IST1 tube, with a luminal surface primarily contributed by basic residues in α1 for membrane binding (17). The different orientations of ESCRT-III proteins against the membrane may indicate that they facilitate membrane abscission through different mechanisms with different topological arrangements.

Deep-etch electron microscopy (DEEM) on the plasma membranes after the overexpressed human Snf7-1 (CHMP4A) and Snf7-2 (CHMP4B) revealed single-stranded filaments that curved and self-associated to create circular arrays (55). More orderly assemblies from yeast Snf7 and worm Vps32 were visualized as flat spirals under atomic force microscopy and cryogenic electron microscopy (cryo-EM), respectively (44, 49). These flat spirals function as the primed state to initiate membrane invagination. DEEM of the plasma membranes after the moderate overexpression of CHMP1B also revealed similar flat spirals, as commonly seen with human Snf7-1 and other well-studied ESCRT-III proteins (17, 56). All these flat spirals comprise highly curved filaments with a small diameter and exhibit a potential preferred orientation on the membrane, making structural determination extremely challenging.

The lack of structural information on ESCRT-III flat spirals hampers the understanding of how ESCRT-III grows into flat spirals and how ESCRT-III flat spirals transform into helical tubes to bend the membranes. Our goal was to tackle the obstacles to reconstructing ESCRT-III flat spirals and unveil their assembly mechanism, which will serve as the initial step in elucidating the molecular mechanisms of ESCRT-mediated membrane remodeling.

Results

Snf7 Flat Spirals on the Membrane. Our previous results have shown that worm Vps32 can self-assemble into single-stranded flat spirals in a head-to-tail mode (49). We are curious whether other ESCRT-III proteins from different species could form similar assemblies in the presence of a membrane. To investigate this, we incubated wild-type yeast Snf7, a model protein of ESCRT-III, at a physiologically relevant concentration of 0.1 mg/mL on top of lipid monolayers to mimic a flat membrane (Fig. 1*A* and *SI Appendix*, Fig. S3*A*). Direct cryo-EM observation revealed that Snf7 did assemble into flat spirals along with a small portion of rings on the lipid monolayers (Fig. 1*B*). This finding is consistent with the results revealed from other species (49, 55, 56), which indicates that the formation of flat spirals is a common feature of ESCRT-III proteins.

Snf7 flat spirals and rings are made of a single-stranded filament with a fixed width of ~4.1 nm (*SI Appendix*, Fig. S3*B*). Snf7 flat spirals exhibit heterogenous overall architectures, with the outer and inner diameters of ~155 ± 70 and 30 ± 5 nm, respectively (Fig. 1*C*). In contrast, Snf7 rings have a tight diameter range between 35 and 45 nm (Fig. 1*C* and *SI Appendix*, Fig. S3*C*), quite close to the inner diameter of the flat spirals. The co-occurrence of Snf7 flat spirals and small rings implies that Snf7 assembly steps from the inner part instead of the outer part (Fig. 1*C*), agreeing with the fluorescence results (44). During the assembly, a closed ring can form when the last Snf7 monomer has sufficient time to meet the start. Otherwise, growth continues into open-ended flat spirals. This process depends on the assembly kinetics, which is highly dependent on Snf7 concentration. Indeed, decreasing Snf7 concentration (~0.05 mg/mL) on top of the lipid monolayers led to more ring formation (*SI Appendix*, Fig. S3*C*).

Irrespective of protein concentration, the membrane is always a requisite for Snf7 assembly. No Snf7 flat spirals or rings are visible under negative stain EM without the lipid monolayers (*SI Appendix*,

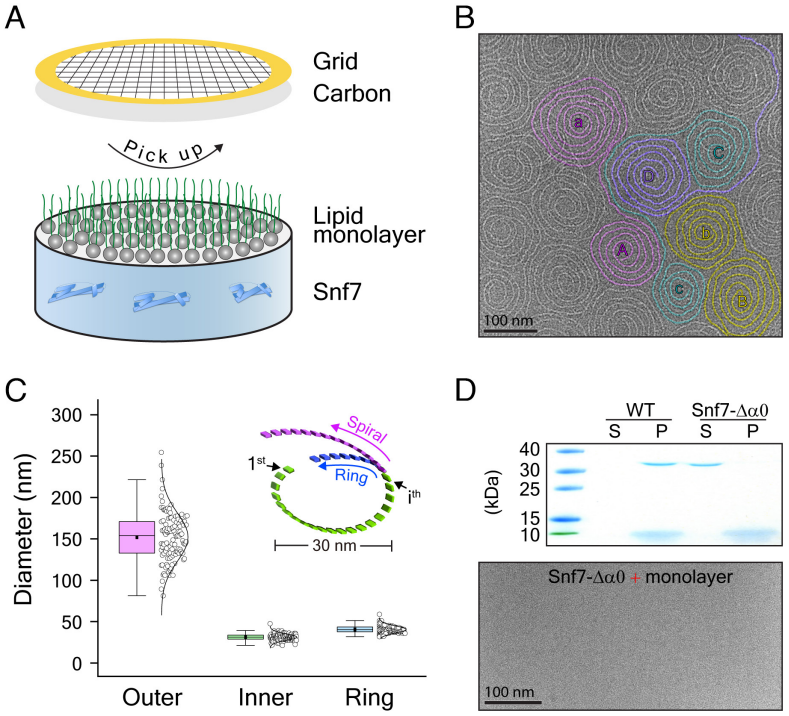

Fig. 1. Wild-type Snf7 assembles into flat spirals on lipid monolayers. (*A*) The schematic diagram on how to incubate Snf7 proteins on lipid monolayers and how to pick up the lipid monolayers using cryo-EM grids. (*B*) A representative cryo-EM micrograph of Snf7 flat spirals on the membrane. Two spirals from the same spiral pair are labeled with the same letter in different cases. (*C*) Diameter distribution of Snf7 flat spirals and rings. The *Inset* shows the assembly from the inner part into either closed rings or open-ended spirals. (*D*) The assembly of Snf7 flat spirals requires the interaction between α0 and membrane. S, supernatant; P, pellet.

Fig. S3*D*), unlike worm Vps32 (49). Snf7 utilizes its N-terminal motif α0 (residues 1 to 11) as the major component to interact with a membrane (57). We removed α0 from wild-type Snf7 (Snf7-Δα0) and found that Snf7-Δα0 did lose the membrane binding ability and could not assemble into either flat spirals or rings even with lipid monolayers present (Fig. 1*D*). All these verify that the α0-membrane interaction is crucial for the assembly of Snf7 flat spirals and rings.

Euler Angle–Assigned Reconstruction. As the primed state, flat spirals are critical to understanding how ESCRT-III transforms into a conical spiral or helical tube during membrane abscission. Due to the tremendous structural heterogeneity, we could not directly perform conventional single-particle cryo-EM on the whole Snf7 flat spirals. The alternative strategy is partitioning Snf7 flat spirals into small fragments and treating each fragment as a single particle for the three-dimensional (3D) reconstruction. Considering that Snf7 flat spirals are highly curved, we marked their filament trajectories via our home-developed MATLAB-based software (Movie S1), partitioned the filaments evenly after correcting the possible deviations, and utilized the trajectories as the centers for particle picking (49). Direct two-dimensional (2D) classification shows the same view of fragments from the outer to inner parts, which indicates only one orientation of Snf7 relative to the membrane (Fig. 2*A*); thus, ESCRT-III flat spirals do not possess a helical symmetry and cannot be processed via helical reconstruction as actin filaments and amyloid fibrils (58–61).

To obtain side-view information of Snf7 flat spirals, we collected tilted micrographs. We performed patch-based contrast transfer function (CTF) estimation on tilted micrographs to track the defocus variation in the direction perpendicular to the tilt axis. Considering that Snf7 flat spirals usually appear as pairs (Fig. 1*B*), we paid special care during cryo-EM grid loading to maintain the same handedness of the projection images across datasets. Meanwhile, we followed a strict anticlockwise direction to manually mark the entire trajectories of the tilted Snf7 flat spirals, which is essential for the EAAR method subsequently described.

Different box sizes were attempted on the untilted Snf7 flat spirals to balance the signal-to-noise ratio and structural rigidity, and the box size at 16.9 nm can hold five subunits and exhibit ideal structural features after 2D classification (*SI Appendix*, Fig. S4*A*). In 2D classes, neighboring subunits have a distance of 2.9 nm (Fig. 2*A*), quite close to what we reported on worm Vps32 (49). This value was used to calculate the overlapping ratio between adjacent boxes at ~83% via $\frac{16.9\ \text{nm}-2.9\ \text{nm}}{16.9\ \text{nm}}$ during particle extraction of Snf7 flat spirals, and each particle will be centered on one asymmetric unit. Different from untilted particles with only one orientation, tilted particles exhibit diverse views after 2D classification (*SI Appendix*, Fig. S4*B*), and only tilted spirals can provide adequate information for the 3D reconstructions.

After tilting, Snf7 flat spirals will be more condensed in the direction perpendicular to the tilt axis. To guarantee that tilted flat spirals were evenly partitioned, we first projected the trajectories of spirals to the untilted plane via the formula $x' = x_0/\cos\theta$; $y' = y_0$, where θ is the tilt angle at 40° and y-axis is the tilt axis, then performed uniform partition on the untilted trajectories, and finally reprojected the particle centers from the untilted trajectories back to the real tilted plane via the formula $x_{new} = x' \times \cos\theta$; $y_{new} = y'$ (Fig. 2*B*).

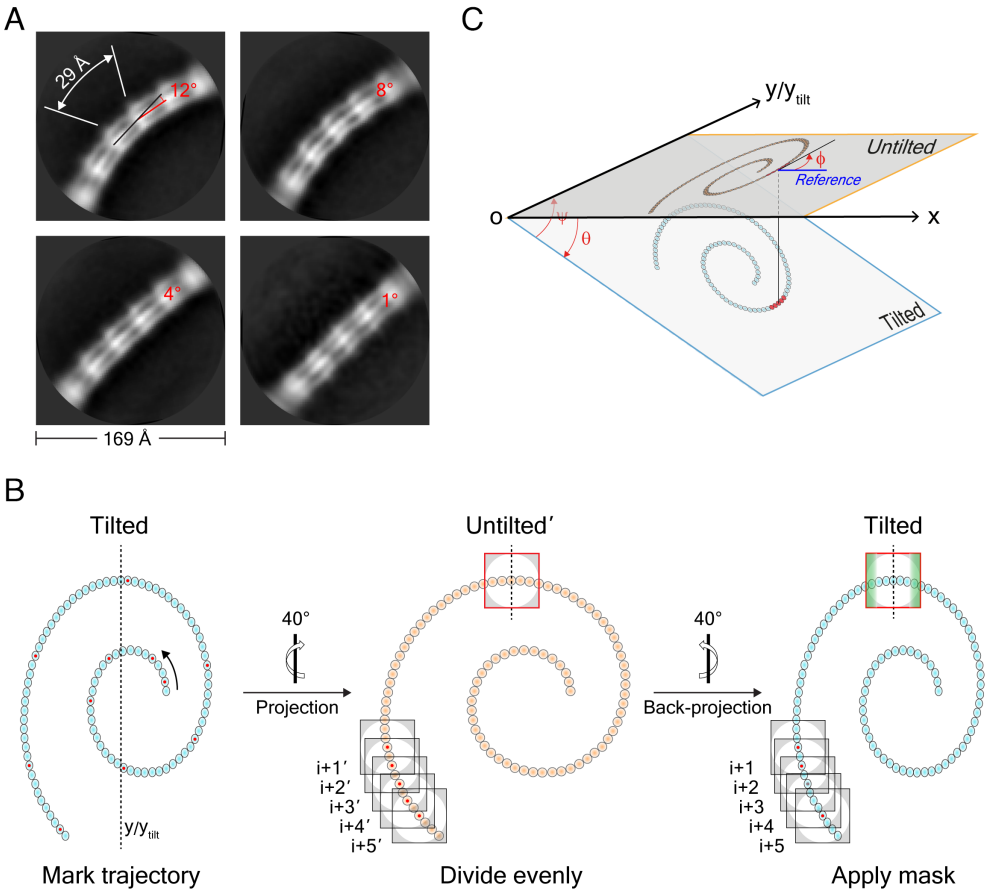

Fig. 2. Euler angle–assigned reconstruction (EAAR) on Snf7 flat spirals. (*A*) 2D class average analyses on untilted Snf7 flat spirals. Classes with varying bending curvatures exhibit only one view. The bending angle between neighboring subunits is labeled in red. (*B*) The schematic diagram to pretreat trajectories of tilted Snf7 flat spirals for ideal particle extraction and masking. Y-axis is the tilt axis, depicted as the dashed lines. (*C*) The schematic diagram on how to obtain three Euler angles of Snf7 flat spirals based on the geometric constraints. The reference is denoted as a blue line parallel to the *x*-axis in the untilted plane.

The x_{new}, y_{new} coordinates were utilized to box tilted flat spirals. To ensure that each tilted particle covers the same number of Snf7 subunits, all extracted particle images were multiplied by a real-space mask whose width is defined as $box\_size \times \cos\theta$ and whose edge is Gaussian blurred (Fig. 2*B*).

Based on the central slice theorem, the vital step for 3D reconstruction is calculating three Euler angles for each particle. We denote the position of a particle by Euler angles ϕ, θ, and ψ, which follows the standard definition of Euler angles for electron microscopy with a specific sequence of intrinsic rotations of the coordinate system (62). Right-handed rotations are designated as positive, and the tangent of the modeled curve is taken to be the x-axis of the reference (*SI Appendix*, Fig. S5).

Inspired by the random conical tilt (RCT) reconstruction method (63), two initial Euler angles for tilted Snf7 flat spirals, θ and ψ, are set at 40° (the tilt angle of micrographs) and −90° (the orientation of the tilt axis), respectively. The sole Euler angle we do not know is the in-plane rotation angle ϕ. Because Snf7 individual particles are boxed from a consecutive filament, the geometric constraint between neighboring particles offered us an opportunity to calculate the rotation angles based on the untilted trajectory of Snf7 flat spirals (Fig. 2*C*). Thus, we can assign all Euler angles to each particle as priors and obtain a 3D structure with only a local angular search. We depict this strategy as EAAR (*SI Appendix*, Fig. S6).

Snf7 Flat Spirals with Varying Curvatures. A total of 1,556,885 particles with the preset Euler angles from Snf7 flat spirals were subjected to multireference 3D classification with the local angular search constrained to ±9°. Two ideal classes were refined into two structures, each comprising five Snf7 subunits (*SI Appendix*, Fig. S6). The middle three subunits were better resolved than the others. We imposed the local symmetry on these three subunits and further refined two structures to better resolutions. The two well-resolved structures exhibit different curvatures, corresponding to the outer and inner parts of Snf7 flat spirals, and were depicted as Snf7-outer and Snf7-inner, respectively (Fig. 3 *A* and *B*).

When calculating the Fourier shell correlation (FSC), we randomly split micrographs into halves. We built two independent particle sets based on micrographs of their origin to ensure that particles originating within the same spiral are contained in the same half-set. Based on the FSC at the criterion of 0.143, Snf7-outer and Snf7-inner were estimated with their respective resolutions at 7.1 and 7.4 Å (*SI Appendix*, Figs. S6 and S7 and Table S1). In Snf7-outer and Snf7-inner, Snf7 subunits assemble in a head-to-tail mode (Fig. 3 *A* and *B*). We performed forward projection on these two structures; the Fourier ring correlation (FRC) analyses showed that their projections matched the direct 2D classifications of the tilted Snf7 flat spirals to a resolution of ~10 Å (*SI Appendix*, Fig. S8), which verifies the internal consistency of the reconstruction with the 2D classes.

Similar to other ESCRT-III proteins, α-helices comprise the major structural elements of Snf7, as revealed by X-ray crystallography (*SI Appendix*, Fig. S2*D*) (17, 37, 42, 64, 65), allowing accurate docking of the Snf7 atomic model (PDB ID 5FD9) into our moderate-resolution cryo-EM maps (Fig. 3 *A* and *B*). In Snf7-outer and Snf7-inner, helices α2 and α3 (residues 60 to 118) merge into a single 9.1 nm long α2/3 helix, indicating an open conformation

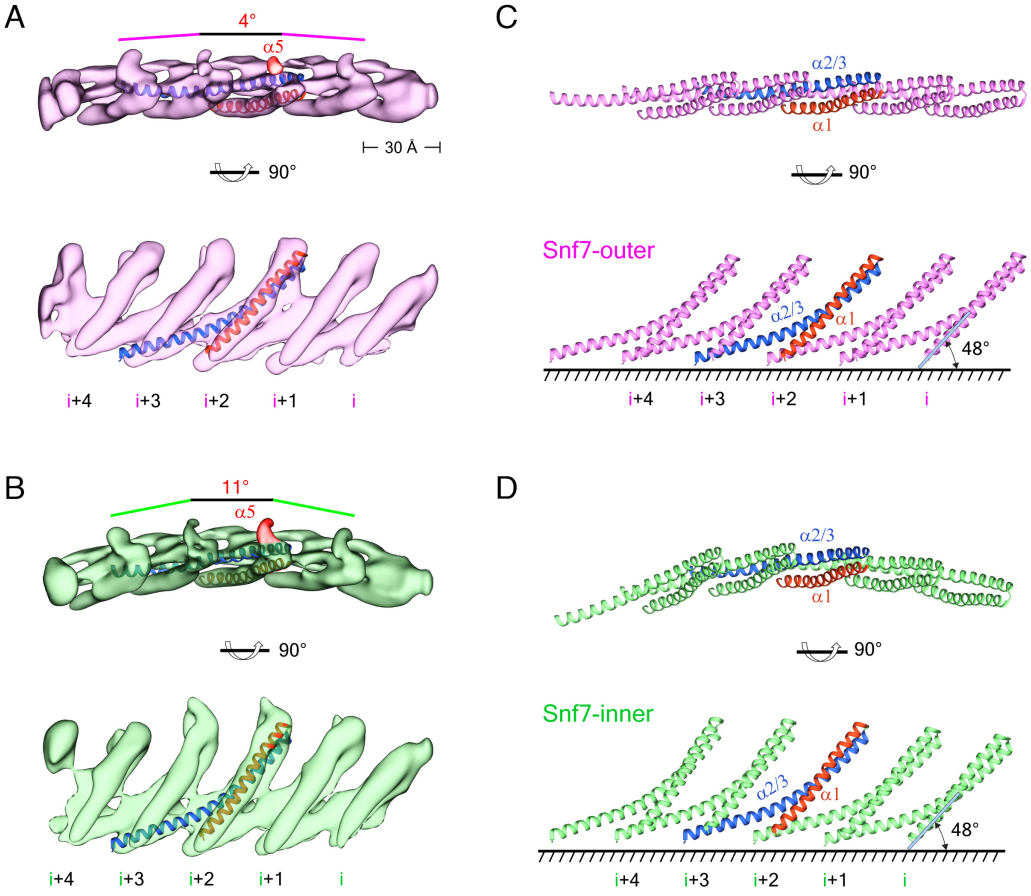

Fig. 3. 3D architectures of Snf7 flat spirals and their atomic models. (*A* and *B*) Cryo-EM maps of the outer (Snf7-outer) and inner (Snf7-inner) parts from Snf7 flat spirals. Snf7-outer and Snf7-inner are colored in purple and green, respectively. EM densities corresponding to α5 in one Snf7-outer and one Snf7-inner are colored in red. (*C* and *D*) Atomic models of Snf7-outer and Snf7-inner. The middle subunit is colored with α1 in coral and α2/3 in cornflower blue. The membrane position is depicted as a black line. The same color strategy is used throughout the manuscript unless specified.

in the Snf7 flat spirals (Fig. 3 *C* and *D*). α1 (residues 19 to 57) is best resolved in either Snf7-outer or Snf7-inner, forming a hairpin with the fused α2/3 (Fig. 3 *A* and *B*).

Immediately before α1, there is an N-terminal α0, unfortunately, invisible in Snf7-outer and Snf7-inner. Considering that α0 contains bulky hydrophobic residues as the membrane insertion motif (*SI Appendix*, Fig. S9) (57), the Snf7 subunit utilizes α0 as a stable membrane anchor, taking a reclining position on the membrane with an angle of 48° along the trajectory of flat spirals (Fig. 3 *C* and *D*). As a result, α1 consistently lies on the inner side of the curved filaments, while α2/3 faces outward (Fig. 3 *C* and *D*). This orientation of Snf7 flat spirals on the membrane is distinct from the previous speculation that α2/3 contacts the membrane (42). The previous analyses merely relied on the wide distribution of positively charged residues from the resolved α1–α4 while ignoring the structurally unresolved negatively charged C-terminal domain (residues 142 to 240; predicted pI value at 3.9) of Snf7, which may pack against α1–α4.

The assembly mechanism of Snf7 flat spirals. Domain swapping is commonly observed among ESCRT-III proteins to hold neighboring subunits together. In the CHMP1B-IST1 helical tube, CHMP1B α4 and the following linker from the i^{th} subunit fuse into a long helix, delivering its α5 to interact with the tip of α1 and α2 hairpin from the $i+4^{th}$ subunit (17, 66). Although α4 and the linker (residues 119 to 159) are not resolved in either Snf7-outer or Snf7-inner, clear EM densities corresponding to α5 exist in both forms (Fig. 3 *A* and *B* and *SI Appendix*, Fig. S10). In Snf7-outer and Snf7-inner, the linear distances between α3 and α5 among neighboring subunits are approximately 3.6, 5.0, and 6.7 nm, corresponding to "i+2," "i+3," and "i+4" domain swapping (*SI Appendix*, Fig. S10). Supposing α4 and the linker in Snf7 flat spirals assemble into a helix as in CHMP1B, the estimated length will be ~6 nm; thus, Snf7-outer and Snf7-inner most probably adopt an i+3 domain swapping mode, which may differ from CHMP1B.

Compared with the curved Snf7 flat spirals, Snf7 subunits assemble into a straight line in the crystal lattice (42), which we depict as Snf7-straight (Fig. 4*A*). In Snf7-straight, the distance between neighboring subunits is 29 Å, identical to Snf7-outer and Snf7-inner (Fig. 4*B*). Comparison of Snf7-straight with Snf7-outer and Snf7-inner revealed two conserved interfaces between neighboring subunits, including Interface-1 and Interface-2 (Fig. 4*B* and *SI Appendix*, Fig. S11). However, the N termini in α2/3 of Snf7-outer and Snf7-inner adopts a distinct conformation from Snf7-straight, with an extra 20° bend away from the membrane (Fig. 4*C*). This bending occurs mainly around E85–Q89 on α2/3, has little effect on Interface-1, but substantially weakens Interface-2 in Snf7-outer and Snf7-inner due to the increased distance compared with Snf7-straight (Fig. 4*B*).

The striking structural difference between Snf7-outer and Snf7-inner comes from α2/3 bending parallel to the membrane

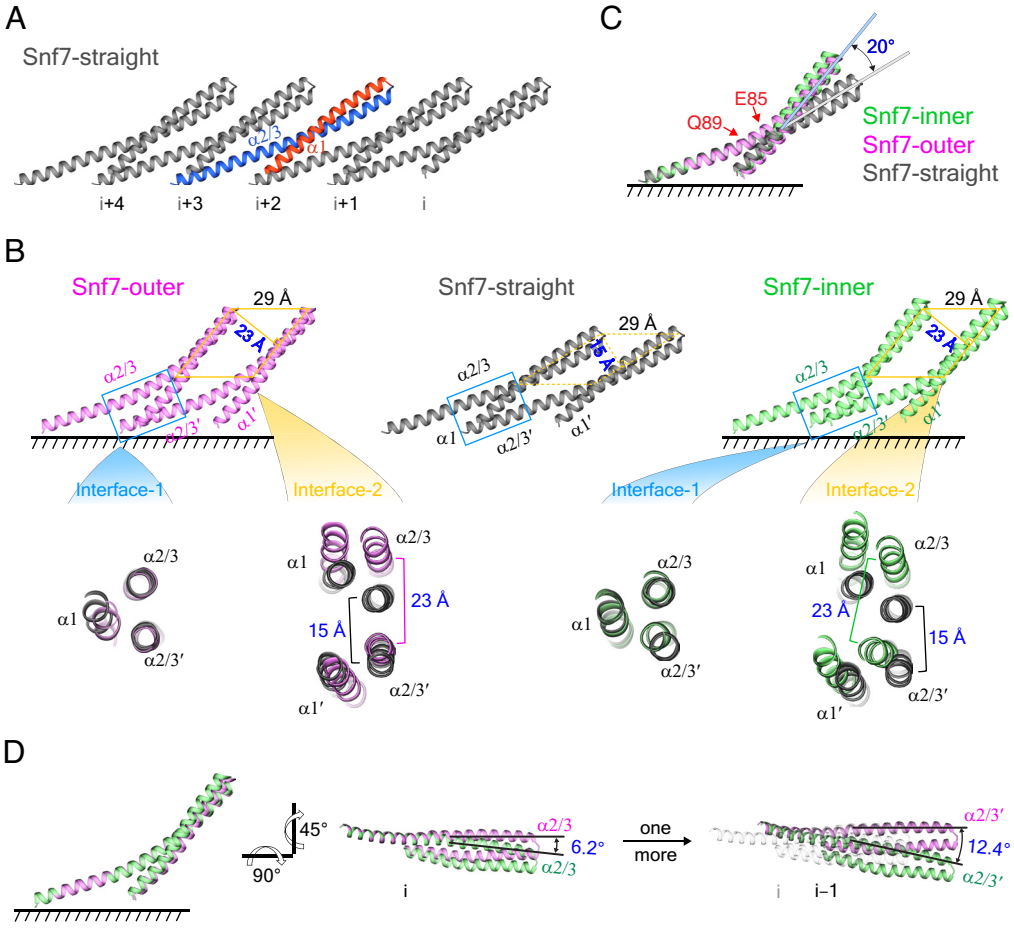

Fig. 4. Molecular mechanisms of Snf7 flat spirals with varying curvatures. (*A*) Atomic model of Snf7-straight with five subunits (PDB ID 5FD9). Only residues from 19 to 118 in each subunit are shown. Four Snf7-straight subunits are colored in gray, and the middle subunit is colored with α1 in coral and α2/3 in cornflower blue. (*B*) Interface comparison of Snf7-outer and Snf7-inner with Snf7-straight. The bending of α2/3 in Snf7-outer has little effect on Interface-1 (marked in a blue rectangle) but abolishes Interface-2 (marked in a yellow parallelogram) due to the increased distance. (*C*) Structural comparison of Snf7-outer and Snf7-inner with Snf7-straight reveals a 20° bending of α2/3 away from the membrane. The hinge region from E85–Q89 is labeled. (*D*) Structural comparison between Snf7-outer and Snf7-inner. α2/3 takes a 6.2° bending from Snf7-outer to Snf7-inner in the plane parallel to the membrane surface.

plane. Specifically, Snf7-inner bends its α2/3 ~6.2° around the residue E85, compared with Snf7-outer (Fig. 4*D*). This fits well with the bending angles of neighboring subunits in Snf7-outer and Snf7-inner at 4° and 11°, respectively (Fig. 3 *A* and *B*). Similar α2/3 bending occurs in other ESCRT-III like CHMP1B and Vipp1 (1, 2). Their α2/3 bend ~6° around the center, which renders CHMP1B helical tube and Vipp1 stacked rings in diameters ranging from 25 to 33 nm (1, 66), analogous to the inner diameter of Snf7 flat spirals—all these point to a conserved mechanism for ESCRT-III to assemble into rings via α2/3 bending.

Discussion

ESCRT-III flat spirals are very peculiar in structure, and their detailed architecture has been elusive for decades, mainly due to the continuous structural heterogeneity and single preferred orientation on the membrane. Using cryo-EM, we collected tilted ESCRT-III flat spirals, partitioned flat spirals into fragments along their trajectory, and assigned all three Euler angles for each fragment as priors for single-particle analyses. We only performed local angular searches during the reconstruction, skipping the conventional global angular search. This EAAR strategy efficiently avoids local minima pitfalls, which helps draw the first picture of ESCRT-III flat spirals on the membrane at the 3D level (Fig. 5).

EAAR derives from the classical RCT, which is widely utilized to obtain reliable initial models (63). RCT requires the acquisition of two micrographs of the same field of view: one tilted and another one untilted. Accordingly, two particle sets will be created with the tilted particles linked to the untilted counterparts. Two Euler angles θ and ψ for each tilted particle can be directly assigned as the known tilt angle of the microscope stage and −90°, respectively. The in-plane rotation angle ϕ of tilted particles needs to be passed from the untilted counterparts after 2D classification. Due to the double exposure issue, RCT is confined mainly to negatively stained samples and will incur severe radiation damage to vitrified ones.

Interestingly, in ESCRT-III flat spirals, subunits are constrained by their trajectories, which offers us an excellent opportunity to calculate in-plane rotation angle ϕ via the constrained trajectories. We projected the tilted trajectories to the untilted plane, calculated the tangent line of each coordinate in the untilted plane, and assigned this angle as the prior of ϕ. Apparently, EAAR combines RCT and geometric constraints of ESCRT-III flat spirals and only needs tilted micrographs, which is ideal for high-resolution cryo-EM. Not limited to the long-sought architecture of the ESCRT-III flat spiral, EAAR can also be broadly applied to complexes, reconstituted vesicles, or cellular organelles where proteins are geometry constrained, overcoming limitations caused by structural heterogeneity and preferred orientation.

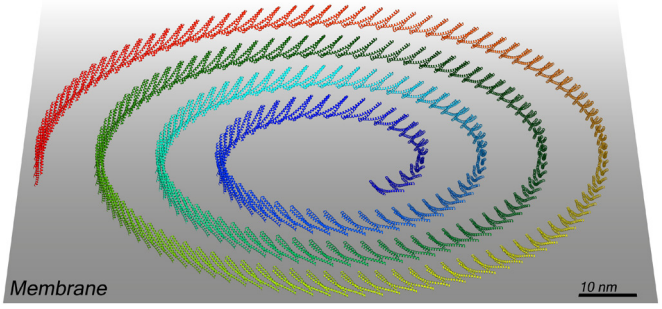

Fig. 5. The pseudoatomic model of ESCRT-III flat spiral on the membrane. ESCRT-III flat spiral visually resembles a clock spring on the membrane. From the outer to inner parts, 250 ESCRT-III subunits are colored in rainbow from red to blue.

Individual ESCRT-III protein is simple in structure with only several helices (67). Via these helices, ESCRT-III can polymerize into flat spirals with continuous bending curvatures, visually like a clock spring (Fig. 5). Via EAAR, we reconstructed two conformations of Snf7 from its flat spirals, representing the outer and inner parts, respectively. Beyond our previous work on worm Vps32 (49), these moderate-resolution Snf7 structures demonstrated orientation and conformations of Snf7 flat spirals on the membrane. They enabled accurate structural comparisons of Snf7-outer and Snf7-inner to unveil the underlying assembly mechanism.

As the primed state of ESCRT-III abscission machinery, understanding how ESCRT-III flat spirals orient against the membrane is critical to elucidating membrane invagination. Here, we observe that Snf7 subunits recline on the membrane, anchored by their α0 helices. As the downstream core subunits of Snf7, human Vps2-Vps24 heterodimers also utilize α0 to interact with the membrane, and the resulting Vps2-Vps24 helical tube is membrane-coated (53). This implies that transitioning from flat spirals to helical tubes does not change the membrane interaction site, with α0 always serving as an anchor. This is distinct from the previous simulation results (68) and provides a clue to understanding the membrane deformation incurred by the structural transition of ESCRT-III.

Due to the tremendous structural heterogeneity along the filament, we could not push Snf7 flat spirals to better resolutions via EAAR. Uniform rings formed by wild-type Snf7 on lipid monolayers are ideal for high-resolution structural determination, providing more structural details about individual Snf7 and their assemblies. Though the most abundant subunit of ESCRT-III machinery, Snf7 alone cannot fulfill the abscission process. Based on Snf7 flat spirals, further studies on Snf7 and the derived complexes formed by Snf7 and Vps2-Vps24 will be helpful to clarify the molecular assembly and possible energy harboring mechanism and to draw a composite model to understand ESCRT-III mediated membrane abscission fully.

Materials and Methods

Protein Expression and Purification. Wild-type Snf7 (NP_013125) was gene synthesized (GENEWIZ, China), and the α0 deletion mutant (Snf7-Δα0) was cloned from the synthesized template using the T7 DNA polymerase protocol. All gene sequences were subcloned into the pET-28b plasmid modified with an MBP-His tag at the N terminus followed by a PreScission Protease (PPase) cleavable site. Four non-native residues (Gly-Pro-Gly-Ser) would be left on Snf7 and Snf7-Δα0 after the PPase cleavage. Both Snf7 and Snf7-Δα0 were heterogeneously expressed in *Escherichia coli* BL21. After the OD_{600} reached ~0.8, cells were induced overnight with 0.5 mM IPTG (isopropylthio-β-galactoside) at 18 °C and harvested via centrifugation at 4 °C.

Cell pellets were resuspended with the lysis buffer (500 mM NaCl, 25 mM Tris-HCl pH 7.6, and 5 mM imidazole) and treated with a protease inhibitor cocktail (Merck). The lysate was centrifuged at 12,000 rpm for 1 h, and the supernatant was incubated with Ni-NTA agarose beads (Qiagen) pre-equilibrated with the lysis buffer. The beads were washed sequentially with the lysis buffer, wash buffer A (150 nm NaCl, 25 mM Tris-HCl pH 7.6, and 10 mM imidazole), and wash buffer B (150 mM NaCl, 25 mM Tris-HCl pH 7.6, and 30 mM imidazole). Then, proteins were eluted with the elution buffer (150 mM NaCl, 25 mM Tris-HCl pH 7.6, and 60 mM imidazole). Eluted proteins were concentrated and mixed with PPase overnight at 4 °C with rotation to cleave the MBP-His tag. The protein solutions were loaded onto the Superdex^{TM} 200 pg column pre-equilibrated with buffer C (100 mM NaCl and 50 mM HEPES pH 7.6). Fractions containing the target proteins were further incubated with fresh Ni-NTA agarose beads (Qiagen) to remove the free MBP-His tag. Tag-free proteins were frozen and stored at −80 °C for future use.

Liposome Sedimentation Assays. Liposomes were prepared using the yeast total lipid (Avanti Polar Lipids). To form a thin lipid film, 50 μL 20 mg/mL total lipid dissolved in chloroform was dried in a vacuum centrifugal concentrator for 4 h. Lipid film was hydrated with 500 μL buffer C and resuspended using sonication until almost clear aqueous dispersion of liposomes was formed. The final concentration of liposomes was 2 mg/mL.

Before the incubation of proteins and liposomes, Snf7 (0.1 mg/mL) and Snf7-Δα0 (0.1 mg/mL) were centrifuged at 15,000 rpm for 10 min to remove possible pellets. Then, 20 μL centrifuged Snf7 or Snf7-Δα0 was mixed with 60 μL liposomes (2 mg/mL) and incubated at room temperature for 30 min. The mixtures were centrifugated at 50,000 rpm for 20 min using a TLA-100 rotor (Beckman). Then, supernatants were gently collected, and pellets were resuspended with 80 μL buffer C. Finally, 40 μL supernatants and redissolved pellets were mixed with 10 μL 5× SDS-loading buffer, heated at 100 °C for 10 min, and subjected to SDS-PAGE gels.

The Lipid Monolayers. To mimic a flat membrane, 18 μL Snf7 or Snf7-Δα0 (concentrations are specified in the main text) was pipetted into the home-made Teflon wells to let the surface bulge out, and 1 μL yeast total lipid (1 mg/mL) was gently added on the surface to form the lipid monolayer. After incubating at room temperature for ~8 h, thin carbon film–coated gold grids (Quantifoil, R2/1, 200 mesh) without glow discharge were utilized to pick up the monolayers bound with Snf7 or Snf7-Δα0 proteins. Some grids were flash-frozen into liquid ethane and then transferred to liquid nitrogen via Vitrobot Mark IV (Thermo Fisher Scientific). Cryo-EM grids were stored in liquid nitrogen for future examination.

Negative Stain EM. Some grids with proteins on lipid monolayers were negatively stained, as described (69). Specifically, ~8 μL uranyl acetate (2%) was applied on grids for staining for 1 min. After removing most stains, the grids were dried in the air. As the control, 4 μL Snf7 (0.1 mg/mL) was directly applied on the glow-discharged carbon-coated grids (400 mesh) and incubated for 1 min. After removing the redundant solution, grids were stained with ~8 μL uranyl acetate for 30 s and then drained with the filter paper. Then, another ~8 μL uranyl acetate was applied on grids for staining for 1 min and drained.

All negatively stained grids were loaded on a Talos L120C (Thermo Fisher Scientific) operated at 120 kV, and images were recorded at the magnification of 57,000× with a Ceta camera (Thermo Fisher Scientific).

Cryo-EM Data Collection. Since Snf7 flat spirals exhibit a single preferred orientation on the membrane and usually appear as pairs, cryo-EM grids were carefully loaded into the autoloader cassette in the same direction to maintain the same handedness of the projection images across datasets. The autoloader cassette was inserted into a Titan Krios G^{3i} (Thermo Fisher Scientific) operated at 300 kV. Both the untilted and tilted data were collected via EPU (Thermo Fisher Scientific), at a nominal magnification of 81,000× with a K3 direct electron detector (Gatan) and GIF Quantum energy filter (slit width of 20 eV) in a super-resolution mode. All movies were collected at a total dose of 50 $e^-/Å^2$ fractionated over 50 frames in a defocus range of −1.2 to −2.4 μm. The super-resolution mode was used with the calibrated pixel size at 0.53 Å. Specifically, 1,988 and 4,629 movies for Snf7 flat spirals were recorded at 0° and 40° tilt angles, respectively. All movies were aligned with MotionCor2 (70), and the contrast transfer function (CTF) parameters were estimated with patch CTF in cryoSPARC 3.1 (71).

3D Reconstructions of Snf7 Flat Spirals.

Particle pretreatments. Snf7 flat spirals exhibit significant heterogeneity in structure and a single preferred orientation on the membrane; thus, we could not perform either helical reconstruction or conventional single-particle cryo-EM on the whole Snf7 flat spirals. The strategy to reconstruct Snf7 flat spirals is partitioning flat spirals into fragments for single-particle analyses. Due to the high curvature, trajectories of flat spirals were manually marked following a strict anticlockwise direction via our home-developed MATLAB-based software as described (49). Then, possible deviations were corrected via the scripts that were also developed in MATLAB. The trajectories were partitioned evenly to obtain the coordinates as the centers for particle picking, with the overlapping ratio between adjacent boxes at ~83%. All these coordinates were passed to Relion 3.1 (72, 73) for 2D classification, 3D classification, and 3D refinement.

A total of 145,178 particles were boxed from the untilted Snf7 flat spirals, using different box sizes such as 325, 169, or 120 Å. Several iterations of 2D classifications were performed on particles in different box sizes, and 169 Å was chosen as the ideal box size after balancing the structural rigidity and signal-to-noise ratio (SNR). Box size at 169 Å was then utilized to extract particles from the tilted Snf7 flat spirals, and the 2D classes exhibited diverse views with strong SNR, which was set for further structural analyses.

For Snf7 flat spirals with the tilt angle at 40°, the trajectories were first projected to the untilted plane along the y-axis using the formula $x' = x_0/\cos 40°;\ y' = y_0$ The projected trajectories were partitioned evenly to obtain new coordinates as the box centers. Meanwhile, the in-plane rotation angle ϕ as the tangent line for each coordinate was calculated based on the geometric constraints from neighboring coordinates. Then, these coordinates from the untilted plane were backprojected via the formula of $x_{new} = x' \times \cos 40°;\ y_{new} = y'$ as the final coordinates for particle extraction from the tilted Snf7 flat spirals. All particle images were multiplied by a real-space mask whose width is $169Å \times \cos 40° = 129Å$ and whose edge is Gaussian blurred. 2,067,353 masked particles were picked up from 4,629 tilted micrographs. The masked particles were subjected to three iterations of 2D classifications. A total of 1,556,885 particles were selected without obvious junks or overlapped filaments.

EAAR. Following the standard definition of Euler angles for electron microscopy (62), we denote the position of a particle by angles ϕ, θ, and ψ, with a specific sequence of intrinsic rotations of the coordinate system. Right-handed rotations are designated as positive. Due to the preferred orientation of Snf7 flat spirals, the tilt angle θ was assigned at 40° to each tilted particle as the prior, and another Euler angle ψ was preset to −90° originating from the orientation of the tilt axis. The in-plane rotation angle ϕ, was calculated as mentioned previously.

Considering that the bending angle between neighboring subunits varies from ~11° to ~4°, we built ten rod-like structures with varying curvature (bending angle between neighboring subunits from 10° to 1°) as initial references in UCSF Chimera. The tangent of the modeled curve is taken to be the x-axis of the reference. Particles with the preset Euler angles (ϕ, 40°, −90°) were subjected to 3D classification against these 10 references. Only local angular search was performed within the scope of ±9° to ensure that Euler angles stay in the correct range. Two ideal classes (Snf7-outer and Snf7-inner) with sufficient map quality represented the outer and inner parts of Snf7 flat spirals, respectively. Particles from each class were chosen for further local refinements.

The reconstructions of Snf7-outer and Snf7-inner comprised five subunits, and the middle three subunits were better resolved. One soft mask was created on one of these three subunits and duplicated to the other two. The local symmetry operators for these three masks were calculated, and the local symmetry was imposed on these three subunits for further refinement in Relion. Resolutions of these two refined reconstructions were estimated via the customized FSC, as described below. We randomly split micrographs into halves to ensure that particles from the same flat spirals are assigned to the same half-set during the FSC calculation. We built two independent particle sets based on micrographs of their origin and obtained their respective 3D reconstructions. For each reconstruction, we merged their own half-maps into an unfiltered full map. We treated these two full maps as the new half-maps, corresponding to two independent particle sets, and calculated the FSC curve between them. The final reconstructions of Snf7-outer and Snf7-inner were estimated at the resolutions of 7.1 Å and 7.4 Å with the criterion of 0.143, respectively.

Due to the single preferred orientation of Snf7 flat spirals, FSC anisotropy analysis was carried out with a 3D-FSC processing server as described (74).

Model Building. The crystal structure of Snf7 (PDB ID 5FD9) was flexibly docked into the maps of Snf7-outer and Snf7-inner in Rosetta (75). Helices α1–α3 (residues from 19 to 118) of Snf7 could fit well into the cryo-EM maps.

The pseudoatomic model of yeast Snf7 in the closed state was modeled from the crystal structures of human CHMP3 (PDB ID 3FRT) (39). The model of Snf7 α0 (residues 2 to 11) was predicted by AlphaFold2 (76).

Structural Analyses. Snf7-straight, Snf7-outer, and Snf7-inner structures were visualized and superimposed with UCSF Chimera (77). The interface analyses were performed in Pisa (https://www.ebi.ac.uk/pdbe/pisa/). The helical wheel on Snf7 α0 was performed in EMBOSS explorer (https://www.bioinformatics.nl/cgi-bin/emboss/pepwheel).

Fourier ring correlation (FRC) was chosen to measure the similarity of the projections of Snf7-outer/Snf7-inner and the 2D classes as a function of spatial frequency. FRC analyses were performed via Fiji (78).

Data, Materials, and Software Availability. The cryo-EM density maps were deposited in Electron Microscopy Data Bank (EMDB, https://www.ebi.ac.uk/pdbe/emdb/) with the accession numbers 37416 (Snf7-outer) (79) and 37417 (Snf7-inner) (80), and their respective fitting structures were deposited in the Protein Data Bank (PDB) with the PDB ID codes 8WB6 (Snf7-outer) (81) and 8WB7 (Snf7-inner) (82). MATLAB codes for particle picking have been uploaded to GitHub: https://github.com/soothing35/EAAR (83). All other data are available in the main text or supporting information.

ACKNOWLEDGMENTS. We are grateful to Kang Li and Dianli Zhao from the Cryo-EM facility for Marine Biology at Qingdao National Laboratory for Marine Science and Technology for our cryo-EM data collection. Q.-T.S. is an investigator of the Institute for Biological Electron Microscopy of Southern University of Science and Technology. This work was supported by the National Key Research and Development Program of China (2021YFF1200400 awarded to Q.-T.S. and Y.W.) and the NSF of China (32170127 awarded to Q.-T.S. and 32371300 awarded to Y.W.).

Author affiliations: [a]School of Life Sciences, Department of Chemical Biology, Southern University of Science and Technology, Shenzhen 518055, China; [b]Laboratory for Marine Biology and Biotechnology, Qingdao Marine Science and Technology Center, Qingdao 266237, China; [c]Institute for Biological Electron Microscopy, Southern University of Science and Technology, Shenzhen 518055, China; [d]iHuman Institute and School of Life Science and Technology, ShanghaiTech University, Shanghai 201210, China; [e]College of Life Sciences, Zhejiang University, Hangzhou 310058, China; [f]The Provincial International Science and Technology Cooperation Base on Engineering Biology, International Campus of Zhejiang University, Haining 314400, China; [g]State Key Laboratory of Microbial Technology, Marine Biotechnology Research Center, Shandong University, Qingdao 266237, China; and [h]Biomedical Research Center for Structural Analysis, Shandong University, Jinan 250012, China

1. J. Liu *et al.*, Bacterial Vipp1 and PspA are members of the ancient ESCRT-III membrane-remodeling superfamily. *Cell* **184**, 3660–3673.e3618 (2021).
2. T. K. Gupta *et al.*, Structural basis for VIPP1 oligomerization and maintenance of thylakoid membrane integrity. *Cell* **184**, 3643–3659.e3623 (2021).
3. B. Junglas *et al.*, PspA adopts an ESCRT-III-like fold and remodels bacterial membranes. *Cell* **184**, 3674–3688.e3618 (2021).
4. A. Spang *et al.*, Complex archaea that bridge the gap between prokaryotes and eukaryotes. *Nature* **521**, 173–179 (2015).
5. K. Zaremba-Niedzwiedzka *et al.*, Asgard archaea illuminate the origin of eukaryotic cellular complexity. *Nature* **541**, 353–358 (2017).
6. T. Hatano *et al.*, Asgard archaea shed light on the evolutionary origins of the eukaryotic ubiquitin-ESCRT machinery. *Nat. Commun.* **13**, 3398 (2022).
7. D. J. Katzmann, G. Odorizzi, S. D. Emr, Receptor downregulation and multivesicular-body sorting. *Nat. Rev. Mol. Cell Biol.* **3**, 893–905 (2002).
8. D. J. Katzmann, M. Babst, S. D. Emr, Ubiquitin-dependent sorting into the multivesicular body pathway requires the function of a conserved endosomal protein sorting complex, ESCRT-I. *Cell* **106**, 145–155 (2001).
9. Y. Takahashi *et al.*, An autophagy assay reveals the ESCRT-III component CHMP2A as a regulator of phagophore closure. *Nat. Commun.* **9**, 2855 (2018).
10. M. Filimonenko *et al.*, Functional multivesicular bodies are required for autophagic clearance of protein aggregates associated with neurodegenerative disease. *J. Cell Biol.* **179**, 485–500 (2007).
11. H. h. Lee, N. Elia, R. Ghirlando, J. Lippincott-Schwartz, J. h. Hurley, Midbody targeting of the ESCRT machinery by a noncanonical coiled coil in CEP55. *Science* **322**, 576–580 (2008).
12. E. Morita *et al.*, Human ESCRT and ALIX proteins interact with proteins of the midbody and function in cytokinesis. *EMBO J.* **26**, 4215–4227 (2007).
13. H. Zhang *et al.*, Endocytic pathways downregulate the L1-type cell adhesion molecule neuroglian to promote dendrite pruning in Drosophila. *Dev. Cell* **30**, 463–478 (2014).
14. N. Loncle, M. Agromayor, J. Martin-Serrano, D. W. Williams, An ESCRT module is required for neuron pruning. *Sci. Rep.* **5**, 8461 (2015).
15. P. D. Bieniasz, Late budding domains and host proteins in enveloped virus release. *Virology* **344**, 55–63 (2006).
16. J. E. Garrus *et al.*, Tsg101 and the vacuolar protein sorting pathway are essential for HIV-1 budding. *Cell* **107**, 55–65 (2001).
17. J. McCullough *et al.*, Structure and membrane remodeling activity of ESCRT-III helical polymers. *Science* **350**, 1548–1551 (2015).
18. R. Allison *et al.*, Defects in ER–endosome contacts impact lysosome function in hereditary spastic paraplegia. *J. Cell Biol.* **216**, 1337–1355 (2017).
19. C. L. Chang *et al.*, Spastin tethers lipid droplets to peroxisomes and directs fatty acid trafficking through ESCRT-III. *J. Cell Biol.* **218**, 2583–2599 (2019).
20. F. D. Mast *et al.*, ESCRT-III is required for scissioning new peroxisomes from the endoplasmic reticulum. *J. Cell Biol.* **217**, 2087–2102 (2018).
21. K. B. Oh, M. J. Stanton, W. W. West, G. L. Todd, K. U. Wagner, Tsg101 is upregulated in a subset of invasive human breast cancers and its targeted overexpression in transgenic mice reveals weak oncogenic properties for mammary cancer initiation. *Oncogene* **26**, 5950–5959 (2007).
22. J. A. Lee, A. Beigneux, S. T. Ahmad, S. G. Young, F. B. Gao, ESCRT-III dysfunction causes autophagosome accumulation and neurodegeneration. *Curr. Biol.* **17**, 1561–1567 (2007).
23. J. McCullough, A. Frost, W. I. Sundquist, Structures, functions, and dynamics of ESCRT-III/Vps4 membrane remodeling and fission complexes. *Annu. Rev. Cell Dev. Biol* **34**, 85–109 (2018).
24. M. S. Kostelansky *et al.*, Molecular architecture and functional model of the complete yeast ESCRT-I heterotetramer. *Cell* **129**, 485–498 (2007).
25. P. S. Bilodeau, S. C. Winistorfer, W. R. Kearney, A. D. Robertson, R. C. Piper, Vps27-Hse1 and ESCRT-I complexes cooperate to increase efficiency of sorting ubiquitinated proteins at the endosome. *J. Cell Biol.* **163**, 237–243 (2003).
26. S. C. Shih *et al.*, Epsins and Vps27p/Hrs contain ubiquitin-binding domains that function in receptor endocytosis. *Nat. Cell Biol.* **4**, 389–393 (2002).
27. T. Slagsvold *et al.*, Eap45 in mammalian ESCRT-II binds ubiquitin via a phosphoinositide-interacting GLUE domain. *J. Biol. Chem.* **280**, 19600–19606 (2005).
28. M. Babst, D. J. Katzmann, W. B. Snyder, B. Wendland, S. D. Emr, Endosome-associated complex, ESCRT-II, recruits transport machinery for protein sorting at the multivesicular body. *Dev. Cell* **3**, 283–289 (2002).
29. H. Teo, O. Perisic, B. Gonzalez, R. L. Williams, ESCRT-II, an endosome-associated complex required for protein sorting: Crystal structure and interactions with ESCRT-III and membranes. *Dev. Cell* **7**, 559–569 (2004).
30. M. Wemmer *et al.*, Bro1 binding to Snf7 regulates ESCRT-III membrane scission activity in yeast. *J. Cell Biol.* **192**, 295–306 (2011).
31. D. P. Dowlatshahi *et al.*, ALIX is a Lys63-specific polyubiquitin binding protein that functions in retrovirus budding. *Dev. Cell* **23**, 1247–1254 (2012).
32. M. Babst, B. Wendland, E. J. Estepa, S. D. Emr, The Vps4p AAA ATPase regulates membrane association of a Vps protein complex required for normal edosome function. *EMBO J.* **12**, 2982–2993 (1998).
33. M. D. Stuchell-Brereton *et al.*, ESCRT-III recognition by VPS4 ATPases. *Nature* **449**, 740–744 (2007).
34. S. Lata *et al.*, Helical structures of ESCRT-III are disassembled by VPS4. *Science* **321**, 1354–1357 (2008).
35. J. h. Hurley, The ESCRT complexes. *Crit. Rev. Biochem. Mol. Biol.* **45**, 463–487 (2010).
36. M. A. Adell, D. Teis, Assembly and disassembly of the ESCRT-III membrane scission complex. *FEBS Lett.* **585**, 3191–3196 (2011).
37. T. Muziol *et al.*, Structural basis for budding by the ESCRT-III factor CHMP3. *Dev. Cell* **10**, 821–830 (2006).
38. J. h. Hurley, P. I. Hanson, Membrane budding and scission by the ESCRT machinery: It's all in the neck. *Nat. Rev. Mol. Cell Biol.* **11**, 556–566 (2010).
39. M. Bajorek *et al.*, Structural basis for ESCRT-III protein autoinhibition. *Nat. Struct. Mol. Biol.* **16**, 754–762 (2009).
40. S. Shim, L. A. Kimpler, P. I. Hanson, Structure/function analysis of four core ESCRT-III proteins reveals common regulatory role for extreme C-terminal domain. *Traffic* **8**, 1068–1079 (2007).
41. A. Zamborlini *et al.*, Release of autoinhibition converts ESCRT-III components into potent inhibitors of HIV-1 budding. *Proc. Natl. Acad. Sci. U.S.A.* **103**, 19140–19145 (2006).
42. S. Tang *et al.*, Structural basis for activation, assembly and membrane binding of ESCRT-III Snf7 filaments. *eLife* **4**, e12548 (2015).
43. B. J. McMillan *et al.*, Electrostatic interactions between elongated monomers drive filamentation of Drosophila shrub, a Metazoan ESCRT-III protein. *Cell Rep.* **16**, 1211–1217 (2016).
44. N. Chiaruttini *et al.*, Relaxation of loaded ESCRT-III spiral springs drives membrane deformation. *Cell* **163**, 866–879 (2015).
45. W. M. Henne, N. J. Buchkovich, Y. Zhao, S. D. Emr, The endosomal sorting complex ESCRT-II mediates the assembly and architecture of ESCRT-III helices. *Cell* **151**, 356–371 (2012).
46. I. Goliand *et al.*, Resolving ESCRT-III spirals at the intercellular bridge of dividing cells using 3D STORM. *Cell Rep.* **24**, 1756–1764 (2018).
47. A. Bertin *et al.*, Human ESCRT-III polymers assemble on positively curved membranes and induce helical membrane tube formation. *Nat. Commun.* **11**, 2663 (2020).
48. J. Moser von Filseck *et al.*, Anisotropic ESCRT-III architecture governs helical membrane tube formation. *Nat. Commun.* **11**, 1516 (2020).
49. Q. T. Shen *et al.*, Structural analysis and modeling reveals new mechanisms governing ESCRT-III spiral filament assembly. *J. Cell Biol.* **206**, 763–777 (2014).
50. J. McCullough, W. I. Sundquist, Membrane remodeling: ESCRT-III filaments as molecular garrotes. *Curr. Biol.* **30**, R1425–R1428 (2020).
51. A. K. Pfitzner *et al.*, An ESCRT-III polymerization sequence drives membrane deformation and fission. *Cell* **182**, 1140–1155.e1118 (2020).
52. G. Fabrikant *et al.*, Computational model of membrane fission catalyzed by ESCRT-III. *PLoS Comput. Biol.* **5**, e1000575 (2009).
53. K. Azad *et al.*, Structural basis of CHMP2A-CHMP3 ESCRT-III polymer assembly and membrane cleavage. *Nat. Struct. Mol. Biol.* **30**, 81–90 (2023).
54. G. Bodon *et al.*, Charged multivesicular body protein 2B (CHMP2B) of the endosomal sorting complex required for transport-III (ESCRT-III) polymerizes into helical structures deforming the plasma membrane. *J. Biol. Chem.* **286**, 40276–40286 (2011).
55. P. I. Hanson, R. Roth, Y. Lin, J. E. Heuser, Plasma membrane deformation by circular arrays of ESCRT-III protein filaments. *J. Cell Biol.* **180**, 389–402 (2008).
56. G. Effantin *et al.*, ESCRT-III CHMP2A and CHMP3 form variable helical polymers in vitro and act synergistically during HIV-1 budding. *Cell Microbiol.* **15**, 213–226 (2013).
57. N. J. Buchkovich, W. M. Henne, S. Tang, S. D. Emr, Essential N-terminal insertion motif anchors the ESCRT-III filament during MVB vesicle formation. *Dev. Cell* **27**, 201–214 (2013).
58. M. Wilkinson *et al.*, Structural evolution of fibril polymorphs during amyloid assembly. *Cell* **186**, 5798–5811.e5726 (2023).
59. C. Röder *et al.*, Cryo-EM structure of islet amyloid polypeptide fibrils reveals similarities with amyloid-β fibrils. *Nat. Struct. Mol. Biol.* **27**, 660–667 (2020).
60. S. Z. Chou, T. D. Pollard, Mechanism of actin polymerization revealed by cryo-EM structures of actin filaments with three different bound nucleotides. *Proc. Natl. Acad. Sci. U.S.A.* **116**, 4265–4274 (2019).

61. E. h. Egelman, The iterative helical real space reconstruction method: Surmounting the problems posed by real polymers. *J. Struct. Biol.* **157**, 83–94 (2007).
62. J. B. Heymann, M. Chagoyen, D. M. Belnap, Common conventions for interchange and archiving of three-dimensional electron microscopy information in structural biology. *J. Struct. Biol.* **151**, 196–207 (2005).
63. M. Radermacher, T. Wagenknecht, A. Verschoor, J. Frank, Three-dimensional reconstruction from a single-exposure, random conical tilt series applied to the 50S ribosomal subunit of *Escherichia coli*. *J. Microsc.* **146**, 113–136 (1987).
64. S. T. Huber, S. Mostafavi, S. A. Mortensen, C. Sachse, Structure and assembly of ESCRT-III helical Vps24 filaments. *Sci. Adv.* **6**, eaba4897 (2020).
65. J. Xiao *et al.*, Structural basis of Ist1 function and Ist1-Did2 interaction in the multivesicular body pathway and cytokinesis. *Mol. Biol. Cell* **20**, 3514–3524 (2009).
66. H. C. Nguyen *et al.*, Membrane constriction and thinning by sequential ESCRT-III polymerization. *Nat. Struct. Mol. Biol.* **27**, 392–399 (2020).
67. A. K. Pfitzner, J. Moser von Filseck, A. Roux, Principles of membrane remodeling by dynamic ESCRT-III polymers. *Trends Cell Biol.* **31**, 856–868 (2021).
68. L. Harker-Kirschneck, B. Baum, A. E. Saric, Changes in ESCRT-III filament geometry drive membrane remodelling and fission in silico. *BMC Biol.* **17**, 82 (2019).
69. N. Zhang *et al.*, Structure and assembly of double-headed Sendai virus nucleocapsids. *Commun. Biol.* **4**, 494 (2021).
70. S. Q. Zheng *et al.*, MotionCor2: Anisotropic correction of beam-induced motion for improved cryo-electron microscopy. *Nat. Methods* **14**, 331–332 (2017).
71. A. Punjani, J. L. Rubinstein, D. J. Fleet, M. A. Brubaker, cryoSPARC: Algorithms for rapid unsupervised cryo-EM structure determination. *Nat. Methods* **14**, 290–296 (2017).
72. S. h. Scheres, RELION: Implementation of a Bayesian approach to cryo-EM structure determination. *J. Struct. Biol.* **180**, 519–530 (2012).
73. J. Zivanov *et al.*, New tools for automated high-resolution cryo-EM structure determination in RELION-3. *eLife* **7**, e42166 (2018).
74. Y. Z. Tan *et al.*, Addressing preferred specimen orientation in single-particle cryo-EM through tilting. *Nat. Methods* **14**, 793–796 (2017).
75. S. Lindert, J. Meiler, J. A. McCammon, Iterative molecular dynamics–Rosetta protein structure refinement protocol to improve model quality. *J. Chem. Theory Comput.* **9**, 3843–3847 (2013).
76. J. Jumper *et al.*, Highly accurate protein structure prediction with AlphaFold. *Nature* **596**, 583–589 (2021).
77. E. F. Pettersen *et al.*, UCSF Chimera–A visualization system for exploratory research and analysis. *J. Comput. Chem.* **25**, 1605–1612 (2004).
78. J. Schindelin *et al.*, Fiji: An open-source platform for biological-image analysis. *Nat. Methods* **9**, 676–682 (2012).
79. M. D. Liu *et al.*, Cryo-EM structure of Snf7 N-terminal domain in outer coils of spiral polymers. EMD. https://www.ebi.ac.uk/emdb/EMD-37416. Deposited 8 September 2023.
80. M. D. Liu *et al.*, CryoEM structure of Snf7 N-terminal domain in the inner coils of spiral. EMD. https://www.ebi.ac.uk/emdb/EMD-37417. Deposited 8 September 2023.
81. M. D. Liu *et al.*, Cryo-EM structure of Snf7 N-terminal domain in outer coils of spiral polymers. PDB. https://www.rcsb.org/structure/unreleased/8WB6. Deposited 8 September 2023.
82. M. D. Liu *et al.*, CryoEM structure of Snf7 N-terminal domain in the inner coils of spiral. PDB. https://www.rcsb.org/structure/unreleased/8WB7. Deposited 8 September 2023.
83. Y. H. Liu *et al.*, EAAR. Github. https://github.com/soothing35/EAAR. Deposited 9 September 2023.